Effect of the Preparation Methods on the Physicochemical Properties of Indium-Based Catalysts and Their Catalytic Performance for

energy&fuels

pubs.acs.org/EF
Article

Effect of the Preparation Methods on the Physicochemical Properties of Indium-Based Catalysts and Their Catalytic Performance for CO_2 Hydrogenation to Methanol

Published as part of Energy & Fuels virtual special issue "Recent Advances in CO2 Conversion to Chemicals and Fuels".

Phuoc Hoang Ho, Giovanni Tizzanini, Sreetama Ghosh, Wei Di, Jieling Shao, Oleg Pajalic, Lars Josefsson, Patricia Benito,* Derek Creaser, and Louise Olsson*

Cite This: https://doi.org/10.1021/acs.energyfuels.3c04721

ABSTRACT: Indium oxides (In_2O_3) and indium oxides supported zirconia (ZrO_2) have been known possible alternatives for conventional copper-based catalysts in the CO_2-hydrogenation to methanol. This study aims to investigate the effect of preparation techniques on the physicochemical properties of indium-based materials and their catalytic performance for the hydrogenation of CO_2 to methanol. Two series of both single oxide In_2O_3 and binary In_2O_3–ZrO_2 have been synthesized by combustion, urea hydrolysis, and precipitation with different precipitating agents (sodium carbonate and ammonia/ethanol solution). Physicochemical properties of materials are characterized by elemental analysis, XRD, N_2 physisorption, SEM/EDX, micro-Raman, XPS, H_2-TPR, and CO_2-TPD. Cubic In_2O_3 was the common phase generated by all four synthesis methods, except for urea hydrolysis, where rhombohedral In_2O_3 was additionally present. The combustion method produced the materials with the lowest specific surface areas while the precipitation using ammonia/ethanol aided in creating more oxygen defects. The synthesis methods strongly influenced the degree of interaction between the oxides and resulted in improvements in properties that boosted the catalytic performance of the binary oxides compared to their single-oxide counterparts.

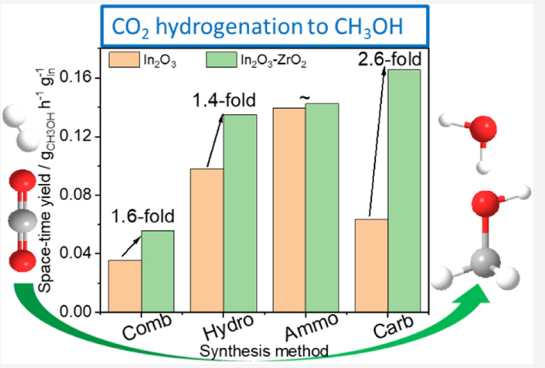

1. INTRODUCTION

Hydrogenation of carbon dioxide into methanol ($CO_2 + 3H_2 \rightleftharpoons CH_3OH + H_2O$, $\Delta H^\circ = -49.4$ kJ mol^{-1}) is one of the interesting processes for the chemical valorization of CO_2 in which a greenhouse gas is transformed into a value-added product.[1] In this process, the methanol product can be further transformed into dimethyl ether, olefins (methanol to olefins, MTO), or gasoline (methanol to gasoline, MTG). Apart from a direct hydrogenation of CO_2 to methanol via the formate intermediate mechanism, the most competitive reaction is the reverse water gas shift ($CO_2 + H_2 \rightleftharpoons CO + H_2O$) which creates CO. This CO intermediate can be further transformed into hydrocarbons via Fischer–Tropsch synthesis as well as oxygenates. As a result, the hydrogenation of CO_2 can produce various products including methanol, carbon monoxide (CO), oxygenates (e.g., dimethyl ether (DME)), and hydrocarbons (HCs).[2] Therefore, developing efficient selective catalysts plays an important role in the production of a target product.

The selection of hydrogenation of CO_2 to methanol is interesting because methanol can be used directly as a solvent or reactant for other industrial chemical production such as formaldehyde, methyl methacrylate, acetic acid, methyl *tert*-butyl ether (MTBE), gasoline blending, and so on.[3] Especially, the use of methanol for sustainable aviation fuels (SAF) production becomes more attractive recently since European Union has recently targeted that 70% of jet fuels at EU airports will have to be green by 2050.[4] There are two directions of methanol conversion to SAF, namely, two-step and one-step (direct) process. For the two-step synthesis, methanol is initially converted into olefins via the MTO process (a combination of reverse water gas shift reaction and Fischer–Tropsch synthesis), and then, the olefin intermediates further oligomerized under conditions that produce olefins in the jet fuel range (C_8–C_{16}). A part of methanol is converted to DME,

Received: November 28, 2023
Revised: February 11, 2024
Accepted: February 12, 2024

which is then transformed over a catalyst to form jet fuel-range hydrocarbons and aromatics.[5] The direct hydrogenation of CO_2 (one step) to long-chain olefins (C_8−C_{16}) is a hot research topic and more challenging due to a quick deactivation of the catalysts by coke formation.[6] However, with an urgent need for SAF production, the production of SAF from CO_2 via methanol production has gained more attention because this process can take advantage of knowledge of MTO and methanol production. In this project, we focused on the first step, namely, the conversion of CO_2 to methanol. Finding a long-term stable catalyst for CO_2 hydrogenation to methanol is still challenging.

In 2013, using DFT calculation, Ye and co-workers found that In_2O_3 would be a potential catalyst for CO_2 hydrogenation to methanol because it can suppress the reverse water gas shift reaction (RWGS) and subsequently increase the selectivity for methanol.[7] The prediction was quickly supported by experimental data in 2015.[8] In 2016, Martin et al. confirmed again the activity of bulk In_2O_3, and they also found that ZrO_2 was the best support for indium-based catalysts among the eight materials investigated (ZrO_2, TiO_2, ZnO, SiO_2, Al_2O_3, activated carbon, SnO_2, and MgO).[9] After that, indium-based catalysts have been extensively investigated with a focus on the effect of the promoters and the supports.[10] Indium oxide has a unique characteristic for the activation of both CO_2 and H_2. It has been proposed that under the reaction conditions, hydrogen is first attracted by the surface oxygen and partially reduces the surface of indium oxide, resulting in the formation of under-coordinated indium sites (In_2O_{3-x}) and thus creating oxygen vacancies that attract the insertion of CO_2 (CO_2 activation).[7] After the reaction, the former vacancy site remains filled by an oxygen atom. The recreation of vacancy can be done by the dissociation of hydrogen to form In−H and adjacent In−OH. The elimination of H_2O via hydride transfer from In−H to the −OH group aids in restoring the vacancy.[11]

There are two stable phases of In_2O_3 reported in the literature, namely, body-centered cubic (bcc-, *Ia*3, a = 10.118 Å) and rhombohedral (rh-, $R\bar{3}c$, a = 5.478 and c = 14.51 Å)[12] and the former is the more common structure than the latter. For bare In_2O_3 catalysts, the crystal structure of In_2O_3 influenced the methanol productivity. Shi et al. have recently reported that the rhombohedral (hexagonal as ascribed by the authors) In_2O_3 was more active than cubic In_2O_3 (space-time yield of methanol around 2.35 versus 2.0 mmol g_{cat}^{-1} h^{-1}) and especially the mixed phase exhibited even better performance than the single phase. The authors correlated better activity with improved textural properties, more oxygen vacancy content, and higher strength and adsorption capacity of CO_2.[13] In contrast, in another work, Yang and co-workers found that although the rhombohedral In_2O_3 had higher methanol selectivity than cubic In_2O_3, it showed lower methanol productivity (space-time yield of methanol around 1.8 versus 3.0 mmol g_{cat}^{-1} h^{-1}). The discrepancy between the two studies could be related to the preparation method of the catalysts. For the mechanism, it has been proposed that CO_2 hydrogenation to methanol over In_2O_3 follows the formate pathway.[13]

The supported In_2O_3 with ZrO_2 showed significant improvement in methanol productivity compared to the bare In_2O_3 by boosting the generation of oxygen vacancies, and, in this regard, monoclinic ZrO_2 was superior to its tetragonal phase.[14] Moreover, ZrO_2 can also aid in suppressing the over-reduction of In_2O_3 by the optimization of surface oxygen vacancy of In_2O_3.[15] Tsoukalou et al. confirmed that the In_2O_3/m-ZrO_2 showed not only the highest productivity of methanol but also the most stable activity with time-on-stream.[16] With the support of a powerful technique, operando X-ray absorption spectroscopy, the authors highlighted that in the In_2O_3/m-ZrO_2 catalyst, the solid solution m-ZrO_2:In prevents the over-reduction of In^{3+} to In^0 and subsequently against the deactivation of this catalyst. With in situ Raman and quasi-in situ XPS, Yang and co-workers demonstrated that a high dispersion of In−O−In together with the improved electron density of In_2O_3 can promote the dissociation of H_2 and hydrogenation of the formate intermediate to methanol.[17] ZrO_2 plays an important role in the stabilization of the formate intermediate,[18] where the bonding strength between the intermediate and Zr sites should be at a modest degree to boost the hydrogenation of the formate intermediate (producing CH_3OH) rather than the C−O bond cleavage of HCOO* (forming CO).[19]

Because the methanol productivity from CO_2 hydrogenation is strongly influenced by the structure of both the In_2O_3 active phase and ZrO_2 support, the preparation method is expected to have an important role in the development of the catalysts. Yanling and co-workers have recently reported a significant effect of the preparation method for CO_2 hydrogenation to methanol over binary oxides of In_2O_3 and ZrO_2 using four different methods (coprecipitation, precipitation-deposition, ball milling, and incipient wetness impregnation).[20] In the present work, we aim to further complete the puzzle by illustrating the effect of the preparation method on the methanol productivity from CO_2 hydrogenation over first the single oxide and how catalytic performance further changes by interactions with ZrO_2. Two series of single oxide In_2O_3 and binary oxide In_2O_3−ZrO_2 were prepared using various methods including urea combustion, urea hydrolysis, and precipitation/coprecipitation using different agents (ammonia solution and sodium carbonate). The physicochemical properties of these materials were characterized with various techniques such as elemental analysis, X-ray diffraction (XRD), N_2 physisorption, scanning electronic microscopy (SEM), micro-Raman, CO chemisorption, temperature-programmed reduction with H_2 (H_2-TPR), temperature-programmed desorption of CO_2 (CO_2-TPD), diffuse reflectance infrared Fourier transform spectroscopy (DRIFTS), and X-ray photon spectroscopy (XPS). The catalytic performance of CO_2 hydrogenation to methanol was investigated using a fixed-bed reactor at 4 MPa.

2. EXPERIMENTAL SECTION

2.1. Chemicals. $In(NO_3)_3{\cdot}xH_2O$ (≥99.99%, Alfa Aesar), $ZrO(NO_3)_2{\cdot}yH_2O$ (≥99%, Sigma-Aldrich), NH_4OH solution (25%, VWR Chemical), urea (≥99.5%, Sigma-Aldrich), and Na_2CO_3 (≥99.5%, Sigma-Aldrich) were used for the catalyst synthesis. Thermogravimetric analysis (TGA) was used to determine the water content in the $In(NO_3)_3{\cdot}xH_2O$ and $ZrO(NO_3)_2{\cdot}yH_2O$ precursors (Figure S1). The weight loss at 800 °C was 38.7 and 36.4% for the former and the latter, respectively. With the assumption that the product at 800 °C was the pure oxide of In_2O_3 and ZrO_2, the values for x and y were found to be 3.2 and 6.0, respectively.

2.2. Catalyst Preparation. The synthesis protocols were designed to obtain about 4 g of each catalyst containing solely In_2O_3 and mixed oxides of In_2O_3−ZrO_2 (molar ratio 1:1). Three synthesis methods were used including urea combustion, urea hydrolysis, and (co)precipitation with NH_4OH and Na_2CO_3.

https://doi.org/10.1021/acs.energyfuels.3c04721
Energy Fuels XXXX, XXX, XXX−XXX

A total of 8 samples were synthesized, and their acronym names, theoretical compositions, and preparation methods are shown in Table 1.

Table 1. Information on Labels, Theoretical Compositions, and the Preparation Methods of the Catalysts

acronym name	composition	preparation method
I-comb	In_2O_3	urea combustion
I-ammo	In_2O_3	NH_4/EtOH precipitation
I-hydro	In_2O_3	urea hydrolysis
I-carb	In_2O_3	Na_2CO_3 precipitation
IZ-comb	In_2O_3–ZrO_2	urea combustion
IZ-ammo	In_2O_3–ZrO_2	NH_4OH/ethanol precipitation
IZ-hydro	In_2O_3–ZrO_2	urea hydrolysis
IZ-carb	In_2O_3–ZrO_2	Na_2CO_3 precipitation

2.2.1. Combustion with Urea. In the pure In_2O_3 catalyst synthesis, 10.23 g of $In(NO_3)_3{\cdot}xH_2O$ and 8.65 g of urea were mixed with a minimum amount of Milli-Q water in a ceramic crucible and kept under stirring for 1 h. The ratio between urea and indium nitrate precursor corresponded to the fuel-to-oxidizer ratio (φ) of 2, according to the reaction stoichiometry:

$$2In(NO_3)_3 + 5\varphi CH_4N_2O + (\varphi - 1)O_2 \rightarrow In_2O_3 + (5\varphi + 3)N_2 + (3.2 + 10\varphi)H_2O + 5\varphi CO_2$$

After that, the crucible was transferred into an oven and heated from 20 to 500 °C (ramp of 5 °C min^{-1}) and held at 500 °C for 6 h. This synthesis yielded a yellowish In_2O_3 product in the form of a light, fragile, and foamy solid (Figure S2). The catalyst was denoted as I-comb, where "I" stands for In_2O_3 and "comb" represents the combustion method.

The mixed oxide In_2O_3–ZrO_2 was synthesized with the same protocol using 7.08 g of $In(NO_3)_3{\cdot}xH_2O$, 3.39 g of $ZrO(NO_3)_2{\cdot}yH_2O$, and 7.99 g of urea. Now, in addition to the $In(NO_3)_3$ combustion shown above, the $ZrO(NO_3)_2$ combustion occurred with stoichiometry:

$$2ZrO(NO_3)_2 + 5\varphi/3CH_4N_2O + (\varphi - 1)O_2 \rightarrow ZrO_2 + (5\varphi/3 + 1)N_2 + (6 + 10\varphi/3)H_2O + 5\varphi/3CO_2$$

The catalyst was denoted as IZ-comb, where "IZ" stands for In_2O_3–ZrO_2.

2.2.2. Urea Hydrolysis. In a typical synthesis, 10.23 g $In(NO_3)_3{\cdot}xH_2O$ and 25.96 g of urea were mixed with 150 mL of Milli-Q water in a round-bottom flask and kept under stirring for 30 min. The flask was connected to a reflux system and it was heated to 90 °C and kept for 16 h. The milky suspension was centrifugated and washed several times with a total of 1 L of distilled water. The solid product was dried at 80 °C for 16 h and subsequently calcined at 500 °C for 6 h (heating rate 5 °C min^{-1}). The catalyst was denoted as I-hydro, where "hydro" stands for the urea hydrolysis method.

A mixed oxide of the In_2O_3–ZrO_2 catalyst was prepared with a similar protocol using 7.08 g of $In(NO_3)_3{\cdot}xH_2O$, 3.39 g of $ZrO(NO_3)_2{\cdot}yH_2O$, and 29.97 g of urea. This catalyst was denoted as IZ-hydro.

2.2.3. Precipitation Using NH_4OH and Ethanol. In a typical synthesis, 10.23 g precursor of indium was dissolved in 150 mL of Milli-Q water in a beaker and the solution was kept stirring for 30 min. Thereafter, a mixture of NH_4OH solution (25% in water) and absolute ethanol (volume ratio 1:2) was added dropwise into the $In(NO_3)_3$ solution until the pH reached around 9.2. The milky solution was kept under stirring for 30 min and then it was aged at 80 °C for another 30 min. Finally, the solution was centrifugated and washed with 1 L of Milli-Q H_2O. The solid product was dried at 80 °C for 16 h and subsequently calcined at 500 °C for 6 h (5 °C min^{-1}). The catalyst was denoted as I-ammo, where "ammo" stands for the employment of an ammonia solution.

A mixed oxide of In_2O_3–ZrO_2 was synthesized in a similar protocol using 7.08 g of $In(NO_3)_3{\cdot}xH_2O$ and 3.39 g of $ZrO(NO_3)_2{\cdot}yH_2O$. The catalyst was labeled as IZ-ammo.

2.2.4. Precipitation Using Na_2CO_3. One sample containing the mixed oxide of In_2O_3–ZrO_2 was prepared using 7.08 g of $In(NO_3)_3{\cdot}xH_2O$ and 3.39 g of $ZrO(NO_3)_2{\cdot}yH_2O$. The same procedure as the NH_4OH/EtOH precipitation was followed, however, a 1 M solution of Na_2CO_3 was used as the precipitating agent to replace the mixed NH_4OH/EtOH solution. The resulting precipitate was aged at 25 °C for 30 min. After that, the suspension was centrifugated and washed with 4 L of hot water (80 °C), until neutral pH, to remove Na as much as possible. The catalyst was labeled IZ-carb, where "carb" stands for the use of carbonate as a precipitating agent.

Single oxide of In_2O_3 was synthesized using the same protocol but using a solution containing 10.23 g $In(NO_3)_3{\cdot}xH_2O$ in 150 mL of Milli-Q water. The catalyst was denoted as I-carb.

2.3. Characterization Techniques. Thermogravimetric analysis (TGA) of $In(NO_3)_3{\cdot}xH_2O$ and $ZrO(NO_3)_2{\cdot}yH_2O$ were measured using a Mettler Toledo TGA/DSC 3+ instrument in air flow (ramp of 10 °C min^{-1}).

Elemental compositions of the catalysts were analyzed using inductively coupled plasma sector field mass spectrometry (ICP-SFMS). The measurements were performed by ALS Scandinavia (Luleå, Sweden).

X-ray diffraction, X-ray photon spectroscopy, and nitrogen physisorption were analyzed to determine crystallite phase, oxidation states, and specific surface area, respectively. A description of these techniques can be found in our previous work.[21]

Scanning electron microscopy was used to investigate the morphology of the catalysts. High-resolution images were acquired using a JEOL JSM-7800F Prime instrument equipped with an EDX (energy-dispersive X-ray) detector. Raman spectra were recorded using Raman microscope alpha300 R, WITec with a laser source at λ = 532 nm.

CO_2-TPD measurements were performed using a calorimeter (Sensys DSC, SETARAM instrumentation) coupled with a mass spectrometer (HPR-20 QIC, Hidden analytical). The sieved catalyst (50 mg with a particle size of 180–250 μm) was loaded in a quartz fixed-bed tube (4 mm of inner diameter). The sample was pretreated in Ar (20 mL min^{-1}) at 300 °C for 0.5 h and subsequently cooled to 25 °C. A flow of 5000 ppm of CO_2/Ar (20 mL min^{-1}) was introduced to the reactor for 1 h in the adsorption step. After that, the reactor was purged with Ar for 30 min to remove the weakly adsorbed CO_2. Eventually, the reactor was subsequently heated from 25 to 700 °C (with a ramp of 10 °C min^{-1}) and kept at 700 °C for 15 min in Ar flow. CO_2 was tracked by the mass number m/z = 44.

H_2-TPR measurements were performed using the same instrument setup as CO_2-TPD. Approximately 20 mg of the catalyst was pretreated under the same conditions as that of CO_2-TPD. A flow of 1 vol % H_2/Ar (20 mL min^{-1}) was subsequently flown through the reactor at 25 °C for 0.5 h. The reactor was then heated from 25 to 800 °C (10 °C min^{-1}) and held at 800 °C for 15 min in Ar flow. H_2 was tracked by the mass number m/z = 2.

Diffuse reflectance infrared Fourier transform spectroscopy (DRIFTS) spectra were carried out with a Vertex 70 spectrometer using a mercury–cadmium–telluride detector (MCT, cooled by liquid nitrogen). The sample (powder) was loaded into a cell (high-temperature reaction cell purchased from Harrick Praying Mantis). Detailed information on the instrument setup can be found elsewhere.[21] Prior to each experiment, the sample was heated at 400 °C in a pure Ar flow for 30 min and subsequently cooled to 35 °C and held at this temperature for 1 h. A background spectrum was recorded at 35 °C. After that, the sample was exposed to a flow of 2000 ppm of CO_2/Ar for 90 min followed by a flow of pure Ar. The spectra were recorded (every minute) for 100 min as soon as CO_2 gas was flown over the sample. It meant that a total of 100 scans were recorded including 90 scans under CO_2 flow and 10 scans in Ar

https://doi.org/10.1021/acs.energyfuels.3c04721
Energy Fuels XXXX, XXX, XXX–XXX

(purging). The last spectrum (100th scan) of each sample was reported for comparison purposes.

2.4. Catalytic Tests. The catalytic test was performed in a fixed-bed tubular stainless-steel reactor (VINCI Technologies, France, inner diameter × length = 1.27 × 21.5 cm). The reactor's total volume was 12.1 cm^3 and it was vertically positioned, with a thermocouple attached to its bottom that ran up to contact with the catalyst bed. Catalysts (particle sizes of 250 and 500 μm) were used for the activity tests to avoid an excessive pressure drop over the catalyst bed. For comparison purposes, the activity tests were designed by keeping the same amount of In metal (500 mg) in each test sample. This required 605 mg of In_2O_3 and 873 mg of In_2O_3–ZrO_2. The catalyst was diluted with SiC (the same particle size) so that the total mass of the catalytic bed was 1 g. In this way, all tests were performed with the same weight hourly space velocity (WHSV) of 6000 mL $g_{catalyst}^{-1}$ h^{-1} (or 12,000 mL g_{In}^{-1} h^{-1}). After a leak test at 40 bar, the catalyst was heated at 350 °C for 1 h in Ar (150 mL min^{-1}). The feed gas was then switched to a mixture of H_2 and CO_2 (molar ratio of CO_2:H_2 = 1:3, a total flow of 100 mL min^{-1}), and the reactor was pressurized to 40 bar. The catalytic tests were measured at five points of temperatures from 350 to 250 °C (interval step of 25 °C). Three measurements are taken for each temperature point with a total reaction time of approximately 75 min to ensure that the steady state is reached. Detailed information on the analytical method and gas chromatography instrument can be found in our previous study.[22]

The apparent activation energy (E_a) of CO_2 on each catalyst was determined from the slope of the Arrhenius plot in which all points of temperatures were selected at a conversion of CO_2 lower than 20%.[23]

The criteria for the estimation of transport effects (mass and heat) were calculated based on the guideline described elsewhere for the best catalyst (IZ-carb).[24] Detailed calculations can be found in the Supporting Information. It was noted that under the highest conversion of CO_2 on the most active catalyst, the Weisz-Prater and Maers parameters were WP = 0.156 and MP = 0.008, respectively. Since WP < 0.6 and MP < 0.15, both intraparticle and interphase mass transfer limitations could be neglected.

3. RESULTS AND DISCUSSION

3.1. Catalyst Characterization. For each synthesis, the theoretical amount of the materials after calcination is approximately 4.0 g. The urea hydrolysis and coprecipitation (using either NH_4OH or Na_2CO_3) methods provided approximately 3.7–3.9 g of product which corresponded to a yield of 93–98% for both single In_2O_3 and mixed oxides. By contrast, the urea combustion method only produced approximately 2.2 g of the materials (55% yield). The elemental compositions of the mixed oxide catalysts determined by ICP-SFMS are shown in Table 2. For binary In_2O_3–ZrO_2, three samples of IZ-hydro, IZ-ammo, and IZ-carb have the molar ratio of In/Zr ≈ 1.85–2.03 which was very close to the theoretical value of 2.0. Notably, the In/Zr of the IZ-comb was only half of the theoretical value. A significant loss in yield of the I-comb and a low In/Zr of the IZ-comb sample were attributed to a loss of the $In(NO_3)_3$ precursor during the combustion. A quick ignition of the combustion probably induced the evaporation of water carrying along with it some $In(NO_3)_3$ precursor. The content of Na in the IZ-carb was negligible, suggesting that Na_2CO_3 was completely removed during the washing step.

Table 2. Elemental Composition of the Catalysts

catalyst	In/molar %	Zr/molar %	Na/ppm
IZ-comb	48.23	51.77	
IZ-hydro	66.11	33.89	
IZ-ammo	64.91	35.09	
IZ-carb	66.98	33.02	<50

Figure 1 presents the XRD patterns of In_2O_3 and In_2O_3–ZrO_2 prepared by the different synthesis methods. The

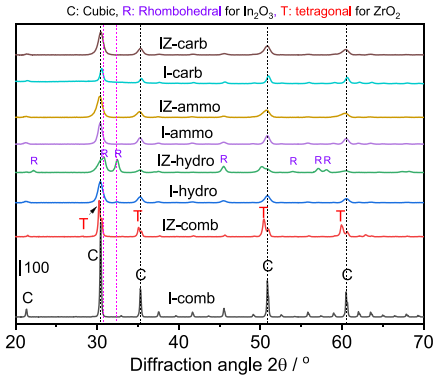

Figure 1. XRD patterns of In_2O_3 and In_2O_3–ZrO_2 prepared by different methods.

reflections of a cubic structure (space group $Ia\bar{3}$ (206), PDF 00-006-0146) were found for all samples of In_2O_3 regardless of the synthesis method, which was in line with the literature.[13] However, the patterns of the In_2O_3 sample prepared by urea hydrolysis showed also weak reflections at around 2θ of 32.5° and 45.6° which were characteristic reflections of the rhombohedral phase (PDF 04-001-8476).[13,25,26] This indicated that the urea hydrolysis method produced a trace of the side phase of the rhombohedral structure apart from the main cubic one. The crystal size of In_2O_3 was calculated with Scherrer's equation using the input information on the plane (431) at 2θ of 45.5°. The result showed that the preparation method significantly influenced the crystallite sizes. The combustion method generated In_2O_3 with a crystallite size of 39 nm (I-comb), which was approximately 3-fold larger than those prepared by other methods, for example, the urea hydrolysis (I-hydro, 12 nm) and precipitation with ammonia (I-ammo, 13 nm) or with Na_2CO_3 (I-carb, 19 nm).

For In_2O_3–ZrO_2 catalysts, IZ-ammo and IZ-carb showed a solid solution of In_2O_3 and ZrO_2 with a cubic structure (like $Zr_{0.18}In_{1.75}O_3$, PDF 04-006-0768) (Figure 1a). This structure was also found in the IZ-hydro sample. However, apart from the cubic structure, the IZ-hydro catalyst also had a rhombohedral phase which was similar to the case of the I-hydro sample. By contrast, the pattern of the IZ-comb showed the reflections assigned to the cubic phase of In_2O_3 as well as the tetragonal ZrO_2 (PDF 00-065-0729).[14] It should be noted that the interpretation of the phase for each In_2O_3–ZrO_2 catalyst was based on a comparison with its In_2O_3 counterpart; however, the interference with the phase of ZrO_2 could not be excluded, especially in the case of the IZ-hydro sample in which the new phase of rhombohedral In_2O_3 was identified. Therefore, four samples of ZrO_2 were prepared with similar methods as the In_2O_3 counterparts, and their XRD patterns are presented in Figure S3. Both Z-hydro and Z-carb showed the same patterns of tetragonal ZrO_2 (PDF 00-065-0729) while Z-ammo and Z-comb exhibited complicated patterns assigned for both tetragonal and monoclinic ZrO_2.[20] A comparison of the patterns of In_2O_3, ZrO_2, and In_2O_3–ZrO_2 samples prepared with the same method was matched to clarify if the patterns of ZrO_2 phases would interfere with the interpretation of the

https://doi.org/10.1021/acs.energyfuels.3c04721
Energy Fuels XXXX, XXX, XXX–XXX

In_2O_3 phases (Figure S4). For the coprecipitation method using sodium carbonate and the urea hydrolysis, the pattern of tetragonal ZrO_2 almost overlapped with the cubic In_2O_3 (Figure S4b,d), and thus, the patterns of In_2O_3−ZrO_2 have likely reassembled the patterns of their In_2O_3 counterparts. In the case of the coprecipitation using ammonia solution, the IZ-ammo showed a very similar pattern with I-ammo, but not with Z-ammo (Figure S4a). The average cell parameter (cubic structure) calculated for two reflections at around 2θ of 30.4° and 35.3° is 10.189 ± 0.005 and 10.211 ± 0.006 Å, respectively. This suggests the formation of a solid solution between In_2O_3 and ZrO_2 in the IZ-ammo reassembled the structure of the I-ammo. For the combustion method, the reflections of the ZrO_2 phase were identified in the pattern of the IZ-comb. The effect of the synthesis methods on the crystallite sizes of In_2O_3−ZrO_2 catalysts was similar to In_2O_3. The IZ-comb showed a large crystallite size of 29 nm whereas the other samples had a size in the range of 12−16 nm. These particle sizes are similar to those we determined in an earlier study, where we analyzed In_2O_3 prepared by the precipitation with Na_2CO_3 using TEM, resulting in particle sizes around 12−16 nm.[22]

Figure 2 displays the SEM images of In_2O_3 and In_2O_3−ZrO_2 catalysts prepared by different methods. The I-comb showed an agglomeration of bent particles, around 200 nm long (Figure 2a). This morphology was also found in the IZ-comb sample, together with well-defined tetragonal crystals (Figure 2b) which belonged to the tetragonal ZrO_2. This is consistent with the XRD data as both the cubic phase of In_2O_3 and tetragonal ZrO_2 were identified from the XRD patterns of the IZ-comb. The indium oxide prepared with the urea hydrolysis—I-hydro was composed of rod particles with a length of approximately 500 nm (Figure 2c) which agrees with the literature.[27] The rod morphology was also partially observed in the IZ-hydro, together with a cluster of ill-defined shapes (Figure 2d). Compared with the phase identified from XRD, it is hypothesized that the rod particles could be associated with the cubic structure of the solid solution of In_2O_3 and ZrO_2, whereas the cluster morphology perhaps belonged to the hexagonal phase (rhombohedral). Both two samples of I-ammo and I-carb showed large clusters with a compact surface (Figure 2e,g). Their In_2O_3−ZrO_2 counterparts, IZ-ammo and IZ-carb, also showed similar morphology; however, the clusters were smaller, and the surface was rougher than I-ammo and I-carb (Figure 2f,h).

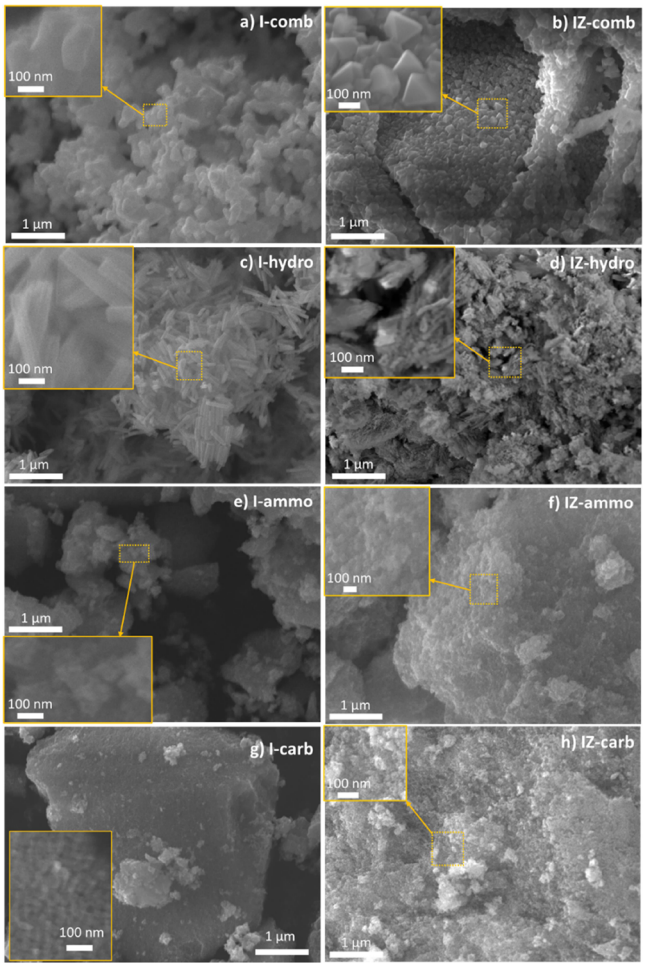

Figure 2. SEM images of In_2O_3 and In_2O_3−ZrO_2 catalysts prepared by different synthesis methods.

More measurements with EDX elemental mapping were performed to examine the distribution of In and Zr elements in In_2O_3−ZrO_2 samples and the results are shown in Figure 3. Overlapping signals of In, Zr, and O were found for the IZ-UH (Figure 3b−b(3)) and IZ-carb (Figure 3c−c(3)), suggesting a homogeneous distribution in the samples. For the IZ-comb sample, the element signals of In and Zr were also overlapping in most of the areas. However, it was noted that at least two areas were characteristics of indium-rich locations as guided by the circles in Figure 3a−a(2). To gain further information, the compositions of eight selected areas on each sample were analyzed by EDX with the point/area mode, and the data are presented in Figure S5. The data for the IZ-comb sample confirmed that there were two areas with indium-rich compositions with In/Zr molar ratios of 6.0−7.0 (points 7 and 8 in Figure S5) while the other 6 points had an average ratio of In/Zr of 1.2 ± 0.1. By contrast, the IZ-hydro and IZ-carb showed similar average ratios of In/Zr around 2.3. Considering that there is a variation in EDX mapping results due to the chosen areas, the In/Zr ratios derived from EDX measurements are consistent with the results of ICP measurements. It would be concluded that the combustion method does not control well the composition of the In and Zr compared to urea hydrolysis and coprecipitation counterparts.

To confirm the presence of different phases of In_2O_3 in the catalysts, micro-Raman measurements were performed, and the results are presented in Figure 4. Five main frequency values of Raman active vibrations were observed in all the spectra at approximately 133 (In−O vibration of InO_6 structure units, E_{2g}), 308 (bending vibration δ (InO_6) of octahedrons, E_{1g}), 369 (stretching vibrations of the In−O−In, E_{2g}), 498 (stretching vibrations ν(InO_6) octahedrons, A_{1g}), and 631 cm^{-1} (ν(InO_6), E_{2g}), which are characteristic of the vibration modes of bcc-In_2O_3 ($Ia3$).[12,28] Moreover, the vibration feature at 369 cm^{-1} also reflects the oxygen vacancies in the In_2O_3 structure.[29] Therefore, a relative ratio of the intensity of this band (I2) and the band at 308 cm^{-1} (I1) is usually used to compare the oxygen vacancy density between the materials.[28] The ratio of I2/I1 was found to be around 0.91−0.96 and 0.71−0.78 for the In_2O_3−ZrO_2 and In_2O_3, respectively (Table 3). This indicated that the presence of ZrO_2 induced an increase in the number of oxygen vacancies compared to the bare In_2O_3. Especially, the Raman shift around 165 cm^{-1} was also observed for the I-hydro and IZ-

https://doi.org/10.1021/acs.energyfuels.3c04721
Energy Fuels XXXX, XXX, XXX−XXX

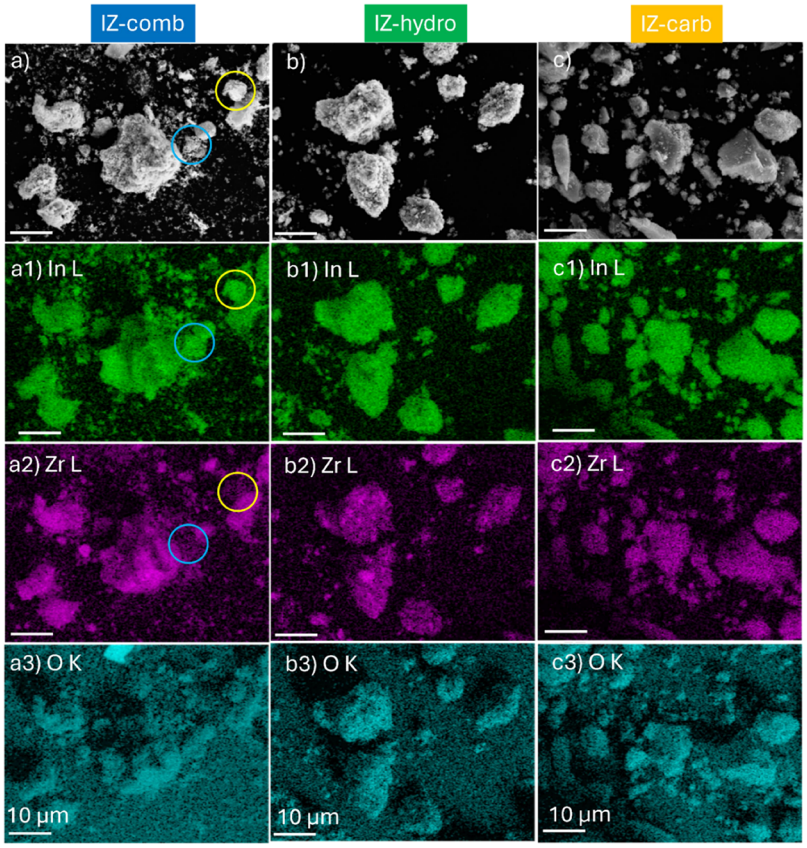

Figure 3. Selected elemental maps of three In_2O_3−ZrO_2 samples from SEM/EDX analysis (IZ-com: a−a3; IZ-hydro: b−b3; and IZ-carb: c−c3): electron images a−c were taken at magnification of 3000. The bar scale in all figures is 10 μm. Maps of In (L): a1, b1, and c1; maps of Zr (L): a2, b2, and c2; and maps of O (K): a3, b3, and c3. The circles in figure a, a1 and a2 mark the indium-rich areas (more detailed information is presented in Figure S6).

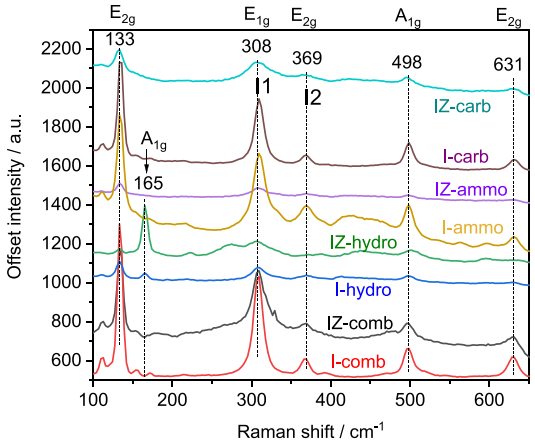

Figure 4. Raman spectra of In_2O_3 and In_2O_3−ZrO_2 catalysts prepared with different methods.

Table 3. Porosity, CO_2 Adsorption Capacity, Crystallite Size, and I2/I1 Ratio of Different Catalysts

catalysts	S_{BET}/m^2 g^{-1}	V_{pore}/cm^3 g^{-1}	CO_2 adsorbed/ μmol g^{-1}	crystallite size[a]/nm	I2/I1[b]
I-comb	4.4	0.008	55	39	0.64
I-hydro	47.4	0.095	149	12	0.95
I-ammo	54.8	0.128	274	13	0.78
I-carb	32.5	0.139	195	19	0.71
IZ-comb	5.2	0.012	78	29	0.80
IZ-hydro	58.4	0.145	242	16	0.91
IZ-ammo	69.6	0.184	399	12	0.96
IZ-carb	69.3	0.298	509	13	0.93

[a]Calculated from the Scherrer equation for the (431) plane. [b]From Raman analysis, where I2 a and I1 are the intensity of the bands at 369 and 308 cm^{-1}, respectively.

hydro samples. This band is characteristic of the rhombohedral structure which was consistent with the XRD data.[25]

Figures S6 and S7 present the N_2-physisorption isotherms of the different catalysts. The isotherms of the two combustion samples (I-comb and IZ-comb) were matched with type II according to the IUPAC classification,[30] indicating a non-porous or macroporous solid. The isotherms of the other catalysts were characteristic of mesoporous materials classified as type IV with the H_2 hysteresis loop. The combustion method generated materials having a specific surface area significantly lower than those prepared by urea hydrolysis and precipitation. The specific surface areas of the I-comb and IZ-comb were 4.4 and 5.2 m^2 g^{-1}, respectively (Table 2). These values were about 10−15-fold lower than those of their counterparts, e.g., 47.4 m^2 g^{-1} of I-hydro and 69.6 m^2 g^{-1} of IZ-ammo. Remarkably, the mixed oxides of In_2O_3−ZrO_2 catalysts always had higher specific surface areas than their In_2O_3 counterparts for all four synthesis methods. This implied that the inclusion of ZrO_2 improved the specific surface area of the catalysts. It is also worth noting that the synthesis method

https://doi.org/10.1021/acs.energyfuels.3c04721
Energy Fuels XXXX, XXX, XXX−XXX

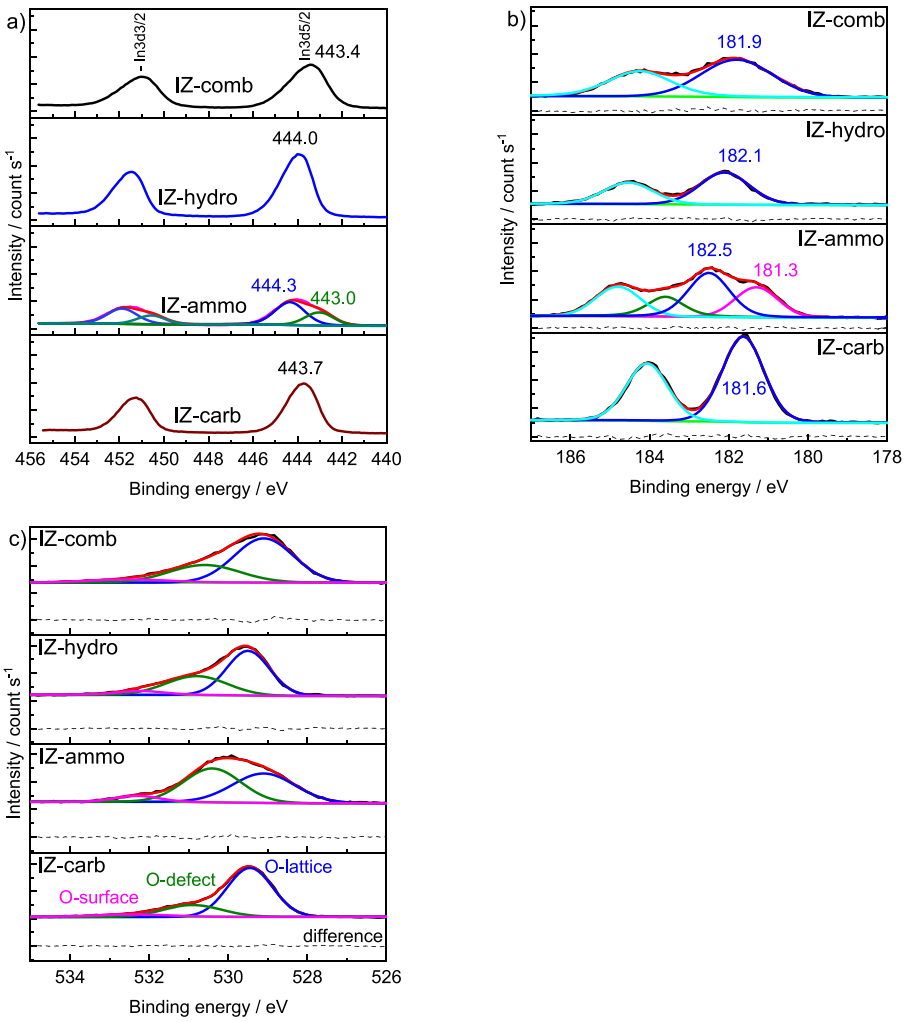

Figure 5. XPS spectra of In_2O_3−ZrO_2 catalysts: (a) In 3d; (b) Zr 3d, and (c) O 1s core level.

significantly influenced the pore size distribution of the materials (Figures S6b and S7b). The average pore size decreased in the order of urea hydrolysis < precipitation with ammonia < precipitation with Na_2CO_3 for both In_2O_3 and In_2O_3−ZrO_2 series.

Figure 5 presents the XPS spectra of In 3d, O 1s, and Zr 3d core levels of different In_2O_3−ZrO_2 catalysts. The In 3d core levels of all samples exhibited two well-separated spin−orbits with a characteristic separation of 7.6 eV between the In 3d5/2 and In 3d3/2 components. The shape of the peaks and the maximum positions of the In 3d5/2 core levels were different between the samples (Figure 5a). The peaks were more asymmetric for IZ-ammo than for the other In_2O_3−ZrO_2 samples. The IZ-comb showed the In 3d5/2 peak at approximately 443.4 eV which was much lower than the value of 443.7 eV for IZ-carb, 444.0 eV for IZ-hydro and 444.3 eV for IZ-ammo. It can be noted that the assignment of the oxidation state for In in In_2O_3 is discrepant in the literature. For example, the database of XPS of the National Institute of Standards and Technology (NIST) assigned a binding energy of In 3d5/2 from 443.2 to 444.0 eV for metallic indium (In^0).[31] In contrast, in the database of Thermofisher, the BEs at 443.8 and 444.0 were assigned to In^0 and In^{3+} (In_2O_3), respectively.[32] It should be noted that the accompanying "loss energy" at around 455−456 eV, a characteristic feature of the metallic indium spectrum, was not observed in any of the four samples. Therefore, it is unlikely to interpret these results as a dominant presence of In^0, for the case of IZ-comb with the lowest BE of In 3d5/2 at 443.4 eV. It should also be noted that with XRD analysis (a technique for bulk analysis) the main phase in these samples was indium oxide, whereas XPS is a surface technique that can analyze the state of material only a few nanometers from the surface. A relatively low value of BE of In 3d5/2 for IZ-comb indicated that there was less electron density around In on the surface (depth up to 5−6 nm, reference[14] and this seemed to be characteristic of the combustion method because the I-comb sample had a similar value of binding energy of In 3d5/2 (443.5 eV) (Figure S8a). Interestingly, the In_2O_3 prepared by thermal decomposition of the $In(NO_3)_3$ precursor also showed a similar value of In 3d5/2 at 443.6 eV in the literature.[33] To clarify that a shift to the lower binding energy of the I-comb sample was not because of the instrumentation issue, we also performed the measurements for other indium oxide samples. As shown in Figure S8a, all three samples (I-hydro, I-ammo, and I-carb) showed a binding energy of In 3d5/2 of around 444.0 eV. We hypothesize that a small fraction of In on the surface of In_2O_3 in the I-comb sample is loosely bonded with oxygen, giving BEs close to metallic In. It should be noted that in the In 3d5/2 of IZ-ammo, the peak at BE of 444.3 eV is the dominant peak at 443.0 eV, indicating that the fraction of the oxide form on the surface of this material was higher than that for the

https://doi.org/10.1021/acs.energyfuels.3c04721
Energy Fuels XXXX, XXX, XXX−XXX

others. This could indicate a strong interaction between In_2O_3 and ZrO_2 due to the formation of a solid solution.

The spectra of the Zr 3d5/2 core level are different among the samples (Figure 5b). Three spectra of IZ-comb, IZ-hydro, and IZ-carb showed a symmetric peak of approximately 181.9, 182.1, and 181.6 eV, respectively, whereas the spectrum of IZ-ammo was broad and asymmetric, which could be deconvoluted into two peaks at 182.5 and 181.3 eV. For four samples, the BE values of the main peaks from 181.6 to 182.4 eV were close to the binding energy of Zr 3d5/2 of tetragonal ZrO_2,[34] in agreement with the XRD data. A deviation of the BEs between the samples indicated a difference in the electron density around Zr^{4+}. The second peak at 181.3 eV in the 3d5/2 spectrum of IZ-ammo indicated the presence of Zr species with less electron density ($Zr^{\delta+}$) which was likely associated with the presence of oxygen defects. It should be noted that the binding energy of Zr 3d of pure ZrO_2 depended on the morphology in which the BE of Zr 3d of monoclinic ZrO_2 was lower than that of tetragonal ZrO_2.[35] It could not be discarded that there is evidence of a trace of a monoclinic phase on the surface because the sample of only ZrO_2 using the same method showed a mixed phase of both monoclinic and tetragonal (Figure S4). Notably, the characteristics of Zr 3d5/2 seemed to coincide with the features of In 3d5/2 of the IZ-ammo, suggesting an interaction between In_2O_3 and ZrO_2 in this sample. Indeed, this interaction was confirmed by the interpretation of the O 1s.

The O 1s spectrum of IZ-ammo showed a significant difference in shape compared to the others (Figure 5c). In the O 1s spectrum, three binding energies at approximately 532.3, 530.5, and 529.1 eV were ascribed to the surface (e.g., −OH group), defect, and lattice oxygen, respectively.[36] Notably, the oxygen defect accounted for 47% of the IZ-ammo which was significantly higher than those for the other three catalysts (23−35%) (Table 4). This result is consistent with the highest

Table 4. Percentage of Different Oxygen (O) Species Deconvoluted from O 1s Binding Energy

sample	lattice O (%)	O-defect (%)	surface O (%)
I-comb	72	17	11
I-hydro	68	21	11
I-ammo	71	17	12
I-carb	75	14	11
IZ-comb	64	30	6
IZ-hydro	59	34	7
IZ-ammo	46	47	7
IZ-carb	71	23	6

content of the defect interpreted from Raman data in which the highest ratio of I2/I1 = 0.96 was found on the IZ-ammo catalyst (Table 3). It is also observed that the ratio between surface −OH and O-defect was significantly different between In_2O_3 and In_2O_3−ZrO_2 counterparts (Table 4). For the In_2O_3 series, the percentage of O-defect and surface −OH was around 14−21% and 11−12%, respectively. Whereas for the In_2O_3−ZrO_2 samples, the former increased by 1.6−2.8-fold while the latter decreased by 1.6−1.8-fold.

Figure 6 presents the H_2-TPR profiles of different catalysts. Pure ZrO_2 showed a negligible consumption of H_2 with a flat profile during the analysis. The profile of all In_2O_3 and In_2O_3−ZrO_2 samples showed only one reduction feature at a high-temperature range of 400−800 °C, whereas the profile of I-

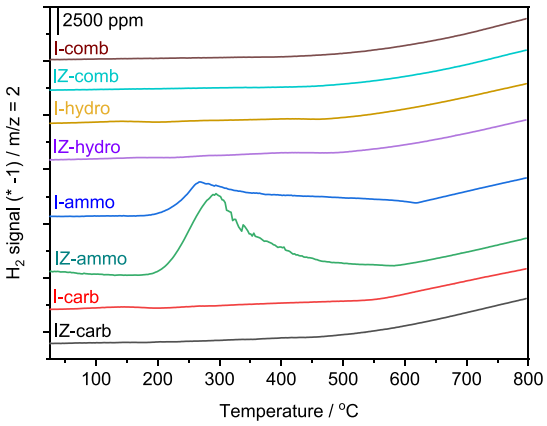

Figure 6. H_2-TPR profiles In_2O_3 and In_2O_3−ZrO_2 prepared by different synthesis methods.

ammo had also another peak at around 270−295 °C. The peak at low temperatures is associated with the reduction of surface In_2O_3 while the peak at high temperatures could be attributed to the reduction of bulk In_2O_3. The profiles of IZ samples showed similar features as their pure In_2O_3 counterparts. The synthesis method using ammonia solution as the precipitating agent facilitates a reduction of In_2O_3 at lower temperatures, contrary to all the other preparation methods. The easy reduction at low temperatures for I-ammo and IZ-ammo is perhaps related to their higher content of oxygen defects which is consistent with the Raman and XPS analysis.[14] Additionally, the reduction of ZrO_2 was also negligible compared to In_2O_3 and In_2O_3−ZrO_2 (Figure S9).

Figure 7 presents the CO_2-TPD profiles for different catalysts. The profile for both I-comb and IZ-comb were

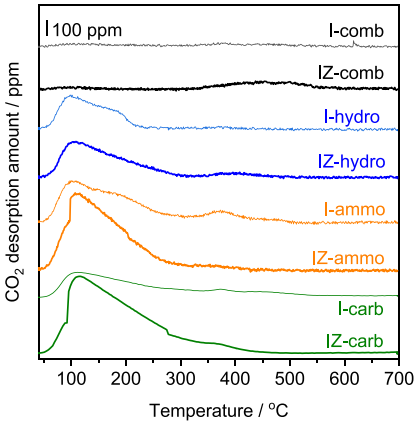

Figure 7. CO_2-TPD profiles of In_2O_3 and In_2O_3−ZrO_2 prepared by different synthesis methods.

almost flat resulting in a small CO_2 uptake of 55 and 78 μmol g^{-1}, respectively. By contrast, the profiles of I-ammo, I-hydro, and I-carb showed one broad peak centered at around 105 °C and one weak peak at around 373 °C. Their CO_2 uptakes were 3-fold to 5-fold higher than that of the I-comb (Table 3). The In_2O_3−ZrO_2 samples had a similar shape of the CO_2-TPD profile to their In_2O_3 counterparts; however, the profiles were more intense. As a result, the CO_2 uptakes of the IZ samples were about 41−62% higher than those of the pure In_2O_3 counterparts (Table 3). This implies that ZrO_2 supports an

https://doi.org/10.1021/acs.energyfuels.3c04721
Energy Fuels XXXX, XXX, XXX−XXX

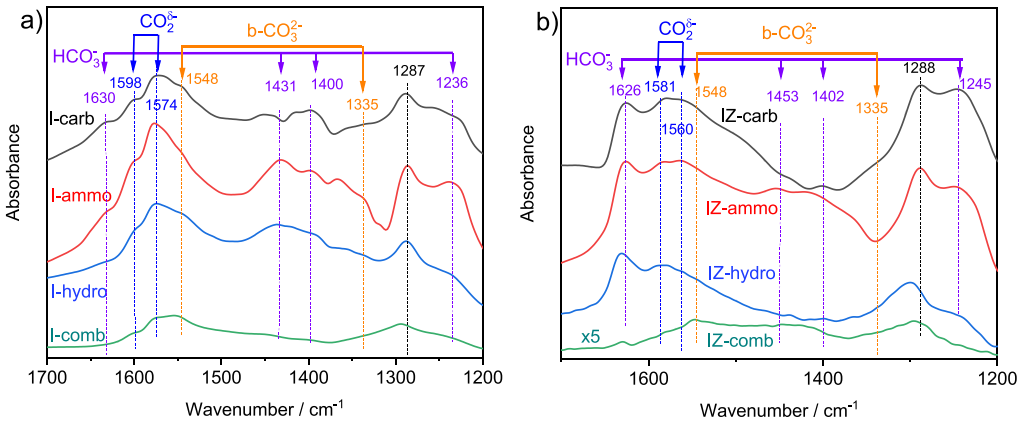

Figure 8. In situ DRIFTS spectra of different catalysts, (a) In_2O_3 and (b) In_2O_3−ZrO_2 after 90 min adsorption of CO_2 at 35 °C (gas flow (100 mL min^{-1}) of 2000 ppm of CO_2/Ar).

enhanced CO_2 adsorption capacity of the mixed oxide catalysts compared to the single In_2O_3 samples.

To gain further information on the structural effect of the catalysts on CO_2 activation, DRIFTS measurements were performed in situ during CO_2 adsorption over the catalysts. Figure 8 presents the IR spectra of In_2O_3 and In_2O_3−ZrO_2 after the adsorption of CO_2 for 90 min. It is known that CO_2 can use its oxygens or electrophilic carbon to interact with the surface −OH and oxygen vacancies of the catalysts in complex coordination (symmetrical, monodente, bidente, and bridged configurations).[37] These interactions possibly form bicarbonates, carbonates, carboxylates, and linear CO_2 species.[38] Different interpretations have been used to assign each species in the literature due to peak overlap and dependence on types of metal oxides. Herein, to simplify the interpretation, we focus on pointing out the different characteristics of the catalysts during CO_2 adsorption to investigate the effect of the catalyst preparation method. As shown in Figure 8a, all spectra showed similar shapes in which the bands positioned at 1630, 1431, and 1236 cm^{-1} can be assigned to bicarbonate (HCO_3^-) with the IR modes of $\nu_{as}(CO_3)$, $\nu_s(CO_3)$, and δ(HO), respectively.[39] The two bands at 1598 and 1574 cm^{-1} are possibly attributed to two types of carboxylate species ($CO_2^{\delta-}$), while the bands at around 1548 and 1335 cm^{-1} are assigned to bidente carbonate (b-CO_3^{2-}).[38,40] It should be noted that the overlap of the peaks in the locations around 1600 cm^{-1} makes it challenging to assign the species. Indeed, the bands at 1598 and 1574 cm^{-1} can be also assigned to formate intermediate species or bidente carbonates in the literature.[19,40] Additionally, there was one intense peak at around 1287 cm^{-1} which was also observed by Yan et al. for CO_2 adsorption on indium oxide.[41] Unfortunately, the authors did not assign this peak. However, this peak can possibly belong to bidente carbonates as reported for CO_2 adsorption on Ni/CeO_2.[42] The spectrum of the I-comb sample was much less intense than the others, probably due to the low specific surface area and hence the low adsorption capacity of CO_2 on this catalyst.

The spectra for the binary oxides In_2O_3−ZrO_2 also showed similar carbonate species as those of In_2O_3 samples, although there were some shifts in the peak positions. This can be explained by a difference in electron density due to the presence of ZrO_2. However, the most different characteristic was the peak at around 1626 cm^{-1}. It was much more intense for In_2O_3−ZrO_2 than the In_2O_3 counterpart. This indicates that more bicarbonate species (HCO_3^-) were formed on In_2O_3−ZrO_2 than In_2O_3 during the CO_2 adsorption.

3.2. Catalytic Activity. The catalytic activity of the different catalysts for CO_2 hydrogenation was examined in a fixed-bed reactor operated in a temperature range from 250 to 350 °C and pressure of 40 bar. The mass of each catalyst was normalized to obtain the same amount of 500 mg of indium for comparison purposes. In all the catalytic tests, CH_3OH and CO were the main products, whereas CH_4 was only found in some cases. In those cases, however, the maximum selectivity of CH_4 was less than 2.5%, and hence, the selectivity for CH_4 is not reported in the results. The comparison of the catalytic activity between the catalysts was assessed in terms of CO_2 conversion (X_{CO2}), CH_3OH selectivity (S_{CH3OH}), and space-time yield of CH_3OH (STY_{CH3OH}).

Figure 9 presents the activity performance (CO_2 conversion, methanol selectivity, and space-time yield of methanol) of In_2O_3 and In_2O_3−ZrO_2 prepared by combustion, urea hydrolysis, and precipitation with NH_4OH solution. More detailed information on methanol yield and CO selectivity are presented in Figure S10. For all catalysts, CO_2 conversion increased substantially as temperature increased from 250 to 350 °C (Figure 9a). For catalysts containing solely In_2O_3, the CO_2 conversion increased in the order of I-comb ≪ I-hydro ≈ I-carb < I-ammo. The CO_2 conversions linearly correlate with the specific surface areas (Figure 10a), suggesting the specific surface area plays a crucial role in the CO_2 conversion since all four catalysts had the same cubic structure of In_2O_3. Significantly lower conversion of CO_2 on the I-comb catalyst was accounted for by a substantially lower specific surface area of the catalyst. It is noted that the CO_2 conversions of I-carb, I-hydro, and I-ammo are better to some extent than those reported in the literature under similar or milder reaction conditions (Table 5). For example, In_2O_3 prepared by the precipitation with Na_2CO_3 showed a conversion of 11.8% at 350 °C under similar reaction conditions,[22] whereas other studies reported much lower CO_2 conversion even under milder reaction conditions (e.g., lower WHSH, reactants diluted with inert gases).[43,44] Both I-hydro and I-ammo catalysts showed a CH_3OH selectivity of 42−45% for temperatures 250−300 °C and the selectivity decreased rapidly with a further increase in temperature due to the RWGS reaction being increasingly thermodynamically favored. The I-comb catalyst also had a similar value of CH_3OH selectivity as I-hydro and I-ammo at temperatures from 250 to 350 °C but it

https://doi.org/10.1021/acs.energyfuels.3c04721
Energy Fuels XXXX, XXX, XXX−XXX

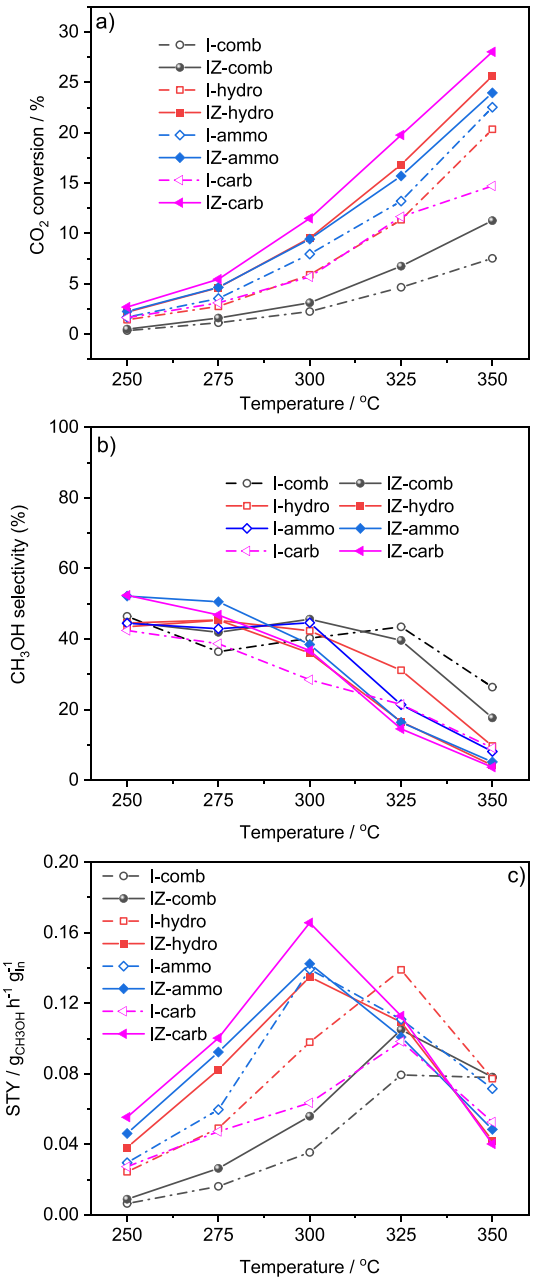

Figure 9. Comparison of In_2O_3 and In_2O_3–ZrO_2 catalysts for (a) CO_2 conversion, (b) CH_3OH selectivity, and (c) STY of CH_3OH.

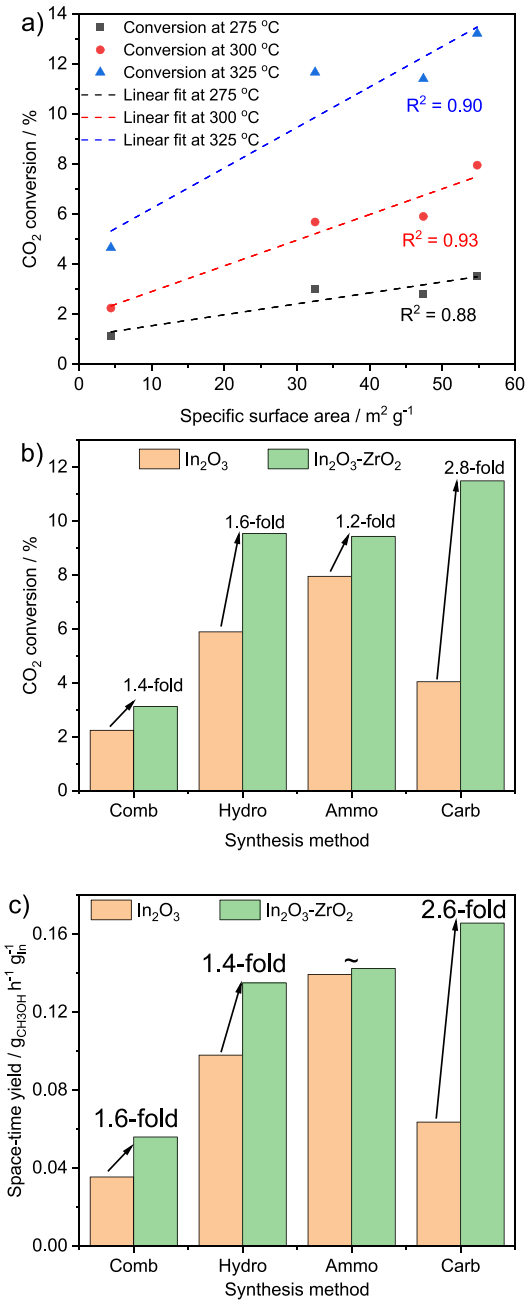

Figure 10. (a) Correlation between the specific surface area and CO_2 conversion on In_2O_3 prepared by various synthesis methods and (b) comparison of CO_2 conversion and (c) comparison of STY of methanol productivity on In_2O_3 and In_2O_3–ZrO_2.

lost CH_3OH selectivity when the temperature was higher than 325 °C. The yield of CH_3OH production on each catalyst is a trade-off between the CO_2 conversion and CH_3OH selectivity (Figure 9b) due to a competition between the methanol generation reaction and the RWGS reaction. As a result, the maximum CH_3OH production rate calculated per gram of Indium (g_{CH3OH} g_{In}^{-1} h^{-1}), i.e. methanol STY, was found to rank in the increasing order of I-comb (0.08 at 325 °C) < I-carb (0.10 at 325 °C) < I-hydro (0.14 at 325 °C) < I-ammo (0.14 at 300 °C) (Figure 9c). This implies that the preparation method strongly influences the catalytic performance for CO_2 hydrogenation to CH_3OH. In the literature, CO_2 conversion, methanol selectivity, and methanol formation are usually correlated to the content of O vacancies;[10,45] however, in this work, the correlation between O vacancies and the methanol production rate was not clear.

Each In_2O_3–ZrO_2 mixed oxide catalyst prepared by the four different methods showed higher CO_2 conversion than that of its In_2O_3 counterpart (Figure 9a, the solid line versus the dashed line with the same color). In particular, the CO_2 conversions on the In_2O_3–ZrO_2 catalysts were 1.2 to 2.8-fold higher than their In_2O_3 counterparts (Figure 10b). This indicates a clear advantage of ZrO_2 support in the mixed oxide In_2O_3–ZrO_2 catalysts, which is generally related to the improvement in CO_2 adsorption capacity and oxygen vacancies of the In_2O_3–ZrO_2 catalysts than their In_2O_3 counterparts.[14,20,29] In fact, in our cases, all samples of binary oxides In_2O_3–ZrO_2 exhibited higher CO_2 adsorption capacity than single In_2O_3 counterparts (Table 3). Moreover, a similar trend

https://doi.org/10.1021/acs.energyfuels.3c04721
Energy Fuels XXXX, XXX, XXX−XXX

Table 5. Comparison of the Activity Performance of the Catalysts Reported in This Study and the Recent Literature

catalysts	CO_2/H_2/inert (v/v)	space velocity		pressure (MPa)	temperature (K)	CO_2 conversion (%)	CH_3OH formation		ref
		GHSV (h^{-1})	WHSV (L g^{-1} h^{-1})				STY (mmol $g_{cat}^{-1}h^{-1}$)	selectivity (%)	
In_2O_3	1/4	16,000	26	5	573		ca. 6.3	100	9
In_2O_3/ZrO_2	1/4	16,000	26	5	573	5.2	9.2	100	9
$In_{2.5}/ZrO_2$	1/4/1.67	24,000		5	523	0.9	1.1	74	18
hexagonal-In_2O_3	1/3/0.55		21.6	4	598	4.4	6.3	68	46
1.5Y9In/ZrO_2	1:4/1.5		52	4	573	7.6	13.1	69	47
3La10In/ZrO_2	1/4/1.5		52	4	573	7.7	13.1	66	47
In_2O_3	1/3/1		9	2	593	~5	14.6	~39	44
20In/ZrO_2-800	1/3/1		9	2	593	~5	59.6	~51	44
c-In_2O_3	1/4/0		16	4	613	~ 12	3.0	20	43
rh-In_2O_3	1/4/0		16	4	613	~ 5	1.8	30	43
In_2O_3-commercial	1/3/1		15	4	543	1.1	0.8	55	8
In_2O_3-commercial	1/3/1		15	4	603	7.1	3.7	40	8
cubic-In_2O_3	1/3/1		7.5	3	573	~4.2	1.99	~70	13
hexagonal-In_2O_3	1/3/1		7.5	3	573	~4.8	2.32	~70	13
In_2O_3-hydro	1/3/0		12	4	598	11.4	3.6	31	this work
In_2O_3–ZrO_2-carb	1/3/0		12	4	573	11.5	3.0	37	this work
In_2O_3–ZrO_2-hydro	1/3/0		12	4	573	9.5	2.4	36	this work

was found for indirect evidence of oxygen vacancies (I2/I1 ratio from Raman analysis) except for the pair of I-hydro and IZ-hydro (Table 3). However, it should be noted that in the case of I-hydro and IZ-hydro, a difference in the phase of In_2O_3 (cubic and rhombohedral, Figure 1a) could play a role in the catalytic activity. IZ-hydro and IZ-ammo catalysts showed very similar CO_2 conversion up to 300 °C but IZ-hydro is slightly better than IZ-ammo at higher temperatures (Figure 9a). Both catalysts outperformed the IZ-comb for the conversion of CO_2 from 250 to 350 °C. Noticeably, the IZ-carb was the best among the four samples of In_2O_3–ZrO_2. This catalyst had 11.5% conversion of CO_2, 37% selectivity for CH_3OH (and hence a maximum 4.2% yield of CH_3OH, Figure S10a) at 300 °C, giving a methanol STY of 0.17 g_{CH3OH} g_{In}^{-1} h^{-1}. The best activity of IZ-carb may be related to its textural properties (Figure 10c), for example, large specific surface area and substantially larger CO_2 adsorption capacity compared to those of the others (see Table 3). Moreover, the pore width (and subsequently the total pore volume) may also play a role because this is the only different textural property between IZ-carb and IZ-ammo, where IZ-carb had 0.298 cm^3 g^{-1} while IZ-ammo had 0.184 cm^3 g^{-1}.

It should be noted that the sodium carbonate precipitation synthesis was the most favorable for the ZrO_2-supported catalyst performance but among the least favorable for the unsupported In_2O_3 catalyst series. A larger crystallite size was found by XRD for I-carb than I-ammo and I-hydro which accounted for a lower specific surface area of I-carb than their counterparts (I-ammo and I-hydro) (Table 3). In the presence of cation Zr^{4+}, all three catalysts prepared by coprecipitation and urea hydrolysis exhibited a high specific surface area, but the difference in the pore width distribution in which the IZ-carb catalyst had a larger value of the average pore width. This indicates that the preparation method significantly influences the CO_2 conversion for In_2O_3–ZrO_2 catalysts. The IZ-hydro and IZ-ammo catalysts showed a maximum rate of CH_3OH STY (at 300 °C) of approximately 0.135 and 0.142 g_{CH3OH} g_{In}^{-1} h^{-1}, respectively, whereas IZ-comb had its maximum rate of CH_3OH STY of about 0.104 g_{CH3OH} g_{In}^{-1} h^{-1} at 325 °C. It is noted that the IZ-hydro had a mixed phase of rhombohedral and cubic In_2O_3 while IZ-ammo possessed only cubic In_2O_3. A slightly higher CO_2 conversion and methanol yield on I-ammo (only cubic phase) than I-hydro (cubic and trace of rhombohedral phase) suggests that the cubic phase of In_2O_3 might be better than the rhombohedral phase as reported in the literature.[13] Yang and co-workers found that the cubic In_2O_3 had a larger production of methanol than rhombohedral unsupported In_2O_3 although the former showed lower methanol selectivity than the latter.[43]

The apparent activation energy of CO_2 on each catalyst was calculated from the slope of the fitted linear regression of the Arrhenius plots, as shown in Figure 11. The apparent activation energies of all catalysts prepared by precipitation and hydrolysis methods were in the range of 71–77 kJ/mol, whereas the values of two samples I-comb and IZ-comb prepared by the combustion method were around 90–91 kJ/mol. This indicates that the pathway of CO_2 activation on the I-comb and IZ-comb was different than other catalysts. The finding was consistent with DRIFTS data in which there were much less $-CO_3$ species formed on I-comb and IZ-comb catalysts during the adsorption of CO_2.

4. CONCLUSIONS

In_2O_3 and In_2O_3–ZrO_2 materials were synthesized by various preparation methods including those with urea and ammonia (free-alkaline) (urea combustion, urea hydrolysis, precipitation with ammonia/ethanol) and the precipitation with sodium carbonate. The preparation methods strongly affected the properties of the catalysts. The combustion method produced a separate phase of ZrO_2 causing a very low specific surface area and, as a result, the catalytic performance of the materials was also limited. A reassembled structure of cubic In_2O_3 for the

https://doi.org/10.1021/acs.energyfuels.3c04721
Energy Fuels XXXX, XXX, XXX–XXX

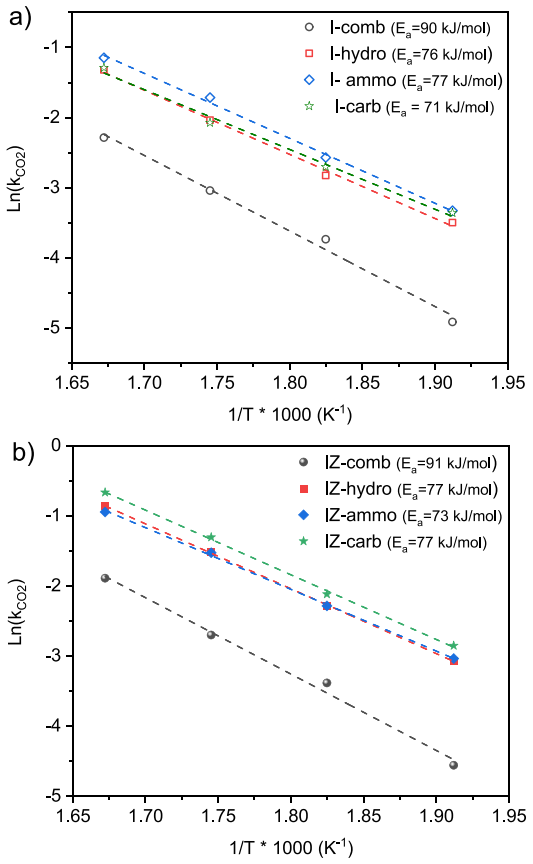

Figure 11. Arrhenius plot for different In_2O_3 and In_2O_3–ZrO_2 catalysts. Apparent activation energy (E_a) was calculated from the slope of the linear regression. All conversion values used in the calculations were lower than 20% to ensure that the selected temperature was in the kinetic range.

In_2O_3–ZrO_2 catalysts prepared by the precipitation with ammonia/ethanol and sodium carbonate indicated a strong interaction between In_2O_3 and ZrO_2. In contrast, the urea hydrolysis method also generated the rhombohedral In_2O_3 structure in both I-hydro and IZ-hydro. The highest content of oxygen defects was found in the In_2O_3–ZrO_2 sample prepared by the precipitation with ammonia/ethanol. However, this factor did not guarantee the best activity performance. The catalytic performance was mostly correlated to the specific surface area. For all preparation methods, the In_2O_3–ZrO_2 mixed oxide catalysts had better performance than their In_2O_3 counterparts. However, using the Na carbonate preparation, the performance was particularly strongly boosted with the mixed oxide. This was due to the IZ-carb catalyst's good textural properties, high CO_2 adsorption capacity, and strong interaction between In_2O_3 and ZrO_2 (as observed from XRD).

■ ASSOCIATED CONTENT

Supporting Information

The Supporting Information is available free of charge at https://pubs.acs.org/doi/10.1021/acs.energyfuels.3c04721.

TGA profiles of $In(NO_3)_3{\cdot}xH_2O$ and $ZrO(NO_3)_2{\cdot}yH_2O$ precursors; Optical image of In_2O_3 prepared by urea combustion method; criteria for estimation of transport effects; XRD data of ZrO_2 samples prepared by different methods; SEM/EDX measurements of selected In_2O_3–ZrO_2 catalysts; N_2 physisorption data of In_2O_3 and In_2O_3–ZrO_2; XPS data of all In_2O_3 samples; H_2-TPR profiles of In_2O_3, ZrO_2, and In_2O_3–ZrO_2 prepared by urea synthesis; and comparison of CH_3OH yield and CO selectivity between In_2O_3 and In_2O_3–ZrO_2 catalysts (PDF)

■ AUTHOR INFORMATION

Corresponding Authors

Patricia Benito − *Dipartimento di Chimica Industriale "Toso Montanari", University of Bologna, Bologna 40136, Italy;* orcid.org/0000-0003-0487-6782; Email: patricia.benito3@unibo.it

Louise Olsson − *Chemical Engineering, Competence Centre for Catalysis, Chalmers University of Technology, Gothenburg SE-412 96, Sweden;* orcid.org/0000-0002-8308-0784; Email: louise.olsson@chalmers.se

Authors

Phuoc Hoang Ho − *Chemical Engineering, Competence Centre for Catalysis, Chalmers University of Technology, Gothenburg SE-412 96, Sweden*

Giovanni Tizzanini − *Dipartimento di Chimica Industriale "Toso Montanari", University of Bologna, Bologna 40136, Italy*

Sreetama Ghosh − *CO2 Research and Green Technologies Centre, Vellore Institute of Technology (VIT), Vellore, Tamil Nadu 632014, India*

Wei Di − *Chemical Engineering, Competence Centre for Catalysis, Chalmers University of Technology, Gothenburg SE-412 96, Sweden*

Jieling Shao − *Chemical Engineering, Competence Centre for Catalysis, Chalmers University of Technology, Gothenburg SE-412 96, Sweden*

Oleg Pajalic − *Perstorp Specialty Chemicals AB, Perstorp 284 80, Sweden*

Lars Josefsson − *Josefsson Sustainable Chemistry AB, Stenungsund 444 48, Sweden*

Derek Creaser − *Chemical Engineering, Competence Centre for Catalysis, Chalmers University of Technology, Gothenburg SE-412 96, Sweden;* orcid.org/0000-0002-5569-5706

Complete contact information is available at: https://pubs.acs.org/10.1021/acs.energyfuels.3c04721

Notes

The authors declare the following competing financial interest(s): Co-author: Oleg Pajalic reports a relationship with Perstorp Specialty Chemicals AB that includes: employment. Co-author: Lars Josefsson, employed by his own company Josefsson Sustainable Chemistry AB.

■ ACKNOWLEDGMENTS

This work was performed at the Competence Centre for Catalysis (KCK) and the Division of Chemical Engineering, Chalmers University of Technology in collaboration with Perstorp, Josefsson Sustainable Chemistry, and Chimica Industriale "Toso Montanari" at the University of Bologna. We thank the Swedish Energy Agency for financial support (Grant number P49617-1). Part of the characterization was conducted at the Chalmers Materials Analysis Lab (CMAL). We acknowledge the assistance from Dr. Eric Tam for XPS analysis and Dr. Katarina Logg for Raman measurements.

https://doi.org/10.1021/acs.energyfuels.3c04721
Energy Fuels XXXX, XXX, XXX−XXX

REFERENCES

(1) Rahman, F. A.; Aziz, M. M. A.; Saidur, R.; Bakar, W. A. W. A.; Hainin, M. R.; Putrajaya, R.; Hassan, N. A. Pollution to solution: Capture and sequestration of carbon dioxide (CO2) and its utilization as a renewable energy source for a sustainable future. *Renewable and Sustainable Energy Reviews* **2017**, *71*, 112−126.

(2) De, S.; Dokania, A.; Ramirez, A.; Gascon, J. Advances in the Design of Heterogeneous Catalysts and Thermocatalytic Processes for CO2 Utilization. *ACS Catal.* **2020**, *10* (23), 14147−14185.

(3) Dalena, F.; Senatore, A.; Marino, A.; Gordano, A.; Basile, M.; Basile, A. Methanol Production and Applications: An Overview. In *Methanol*; Basile, A.; Dalena, F. Eds.; Elsevier, 2018; pp 3−28.

(4) *News European Parliament Home Page*. https://www.europarl.europa.eu/news/en/press-room/20230911IPR04913/70-of-jet-fuels-at-eu-airports-will-have-to-be-green-by-2050 (accessed October 2023).

(5) Bradin, D. Process for producing renewable jet fuel compositions. WO2014008337A1, 2013.

(6) Yao, B.; Xiao, T.; Makgae, O. A.; Jie, X.; Gonzalez-Cortes, S.; Guan, S.; Kirkland, A. I.; Dilworth, J. R.; Al-Megren, H. A.; Alshihri, S. M.; et al. Transforming carbon dioxide into jet fuel using an organic combustion-synthesized Fe-Mn-K catalyst. *Nat. Commun.* **2020**, *11* (1), 6395.

(7) Ye, J.; Liu, C.; Mei, D.; Ge, Q. Active Oxygen Vacancy Site for Methanol Synthesis from CO2 Hydrogenation on In2O3(110): A DFT Study. *ACS Catal.* **2013**, *3* (6), 1296−1306.

(8) Sun, K.; Fan, Z.; Ye, J.; Yan, J.; Ge, Q.; Li, Y.; He, W.; Yang, W.; Liu, C.-J. Hydrogenation of CO2 to methanol over In2O3 catalyst. *Journal of CO2 Utilization* **2015**, *12*, 1−6.

(9) Martin, O.; Martín, A. J.; Mondelli, C.; Mitchell, S.; Segawa, T. F.; Hauert, R.; Drouilly, C.; Curulla-Ferré, D.; Pérez-Ramírez, J. Indium Oxide as a Superior Catalyst for Methanol Synthesis by CO2 Hydrogenation. *Angew. Chem., Int. Ed.* **2016**, *55* (21), 6261−6265.

(10) Wang, J.; Zhang, G.; Zhu, J.; Zhang, X.; Ding, F.; Zhang, A.; Guo, X.; Song, C. CO2 Hydrogenation to Methanol over In2O3-Based Catalysts: From Mechanism to Catalyst Development. *ACS Catal.* **2021**, *11* (3), 1406−1423.

(11) Baumgarten, R.; Naumann d'Alnoncourt, R.; Lohr, S.; Gioria, E.; Frei, E.; Fako, E.; De, S.; Boscagli, C.; Drieß, M.; Schunk, S.; et al. Quantification and Tuning of Surface Oxygen Vacancies for the Hydrogenation of CO2 on Indium Oxide Catalysts. *Chem. Ing. Techn.* **2022**, *94* (11), 1765−1775.

(12) Wang, C. Y.; Dai, Y.; Pezoldt, J.; Lu, B.; Kups, T.; Cimalla, V.; Ambacher, O. Phase Stabilization and Phonon Properties of Single Crystalline Rhombohedral Indium Oxide. *Cryst. Growth Des.* **2008**, *8* (4), 1257−1260.

(13) Shi, Z.; Tan, Q.; Wu, D. Mixed-Phase Indium Oxide as a Highly Active and Stable Catalyst for the Hydrogenation of CO2 to CH3OH. *Ind. Eng. Chem. Res.* **2021**, *60* (9), 3532−3542.

(14) Frei, M. S.; Mondelli, C.; Cesarini, A.; Krumeich, F.; Hauert, R.; Stewart, J. A.; Curulla Ferré, D.; Pérez-Ramírez, J. Role of Zirconia in Indium Oxide-Catalyzed CO2 Hydrogenation to Methanol. *ACS Catal.* **2020**, *10* (2), 1133−1145.

(15) Wu, H.; Xiong, S.; Liu, C.-J. Preparation of In2O3/ZrO2 catalyst via DBD plasma decomposition of Zr(OH)4 for CO2 hydrogenation to methanol. *Catal. Today* **2023**, *423*, 114024.

(16) Tsoukalou, A.; Abdala, P. M.; Armutlulu, A.; Willinger, E.; Fedorov, A.; Müller, C. R. Operando X-ray Absorption Spectroscopy Identifies a Monoclinic ZrO2:In Solid Solution as the Active Phase for the Hydrogenation of CO2 to Methanol. *ACS Catal.* **2020**, *10* (17), 10060−10067.

(17) Yang, C.; Pei, C.; Luo, R.; Liu, S.; Wang, Y.; Wang, Z.; Zhao, Z.-J.; Gong, J. Strong Electronic Oxide−Support Interaction over In2O3/ZrO2 for Highly Selective CO2 Hydrogenation to Methanol. *J. Am. Chem. Soc.* **2020**, *142* (46), 19523−19531.

(18) Chen, T.-Y.; Cao, C.; Chen, T.-B.; Ding, X.; Huang, H.; Shen, L.; Cao, X.; Zhu, M.; Xu, J.; Gao, J.; et al. Unraveling Highly Tunable Selectivity in CO2 Hydrogenation over Bimetallic In-Zr Oxide Catalysts. *ACS Catal.* **2019**, *9* (9), 8785−8797.

(19) Regalado Vera, C. Y.; Manavi, N.; Zhou, Z.; Wang, L.-C.; Diao, W.; Karakalos, S.; Liu, B.; Stowers, K. J.; Zhou, M.; Luo, H.; et al. Mechanistic understanding of support effect on the activity and selectivity of indium oxide catalysts for CO2 hydrogenation. *Chemical Engineering Journal* **2021**, *426*, No. 131767.

(20) Wei, Y.; Liu, F.; Ma, J.; Yang, C.; Wang, X.; Cao, J. Catalytic roles of In2O3 in ZrO2-based binary oxides for CO2 hydrogenation to methanol. *Molecular Catalysis* **2022**, *525*, No. 112354.

(21) Ho, P. H.; Woo, J.-W.; Feizie Ilmasani, R.; Han, J.; Olsson, L. The role of Pd−Pt Interactions in the Oxidation and Sulfur Resistance of Bimetallic Pd−Pt/γ-Al2O3 Diesel Oxidation Catalysts. *Ind. Eng. Chem. Res.* **2021**, *60* (18), 6596−6612.

(22) Ghosh, S.; Sebastian, J.; Olsson, L.; Creaser, D. Experimental and kinetic modeling studies of methanol synthesis from CO2 hydrogenation using In2O3 catalyst. *Chemical Engineering Journal* **2021**, *416*, No. 129120.

(23) Ho, P. H.; Jabłońska, M.; Palkovits, R.; Rodríguez-Castellón, E.; Ospitali, F.; Fornasari, G.; Vaccari, A.; Benito, P. N2O catalytic decomposition on electrodeposited Rh-based open-cell metallic foams. *Chemical Engineering Journal* **2020**, *379*, No. 122259.

(24) Beller, M.; Renken, A.; Van Santen, R. *Catalysis From Principles to Applications*; Wiley-VCH, 2012.

(25) Song, L.; Dou, K.; Wang, R.; Leng, P.; Luo, L.; Xi, Y.; Kaun, C.-C.; Han, N.; Wang, F.; Chen, Y. Sr-Doped Cubic In2O3/Rhombohedral In2O3 Homojunction Nanowires for Highly Sensitive and Selective Breath Ethanol Sensing: Experiment and DFT Simulation Studies. *ACS Appl. Mater. Interfaces* **2020**, *12* (1), 1270−1279.

(26) Gao, L.; Ren, F.; Cheng, Z.; Zhang, Y.; Xiang, Q.; Xu, J. Porous corundum-type In2O3 nanoflowers: controllable synthesis, enhanced ethanol-sensing properties and response mechanism. *CrystEngComm* **2015**, *17* (17), 3268−3276.

(27) Zhu, H.; Wang, X.; Yang, F.; Yang, X. Template-Free, Surfactantless Route to Fabricate In(OH)3 Monocrystalline Nanoarchitectures and Their Conversion to In2O3. *Cryst. Growth Des.* **2008**, *8* (3), 950−956.

(28) Gan, J.; Lu, X.; Wu, J.; Xie, S.; Zhai, T.; Yu, M.; Zhang, Z.; Mao, Y.; Wang, S. C. I.; Shen, Y.; et al. Oxygen vacancies promoting photoelectrochemical performance of In2O3 nanocubes. *Sci. Rep.* **2013**, *3* (1), 1021.

(29) Frei, M. S.; Capdevila-Cortada, M.; García-Muelas, R.; Mondelli, C.; López, N.; Stewart, J. A.; Curulla Ferré, D.; Pérez-Ramírez, J. Mechanism and microkinetics of methanol synthesis via CO2 hydrogenation on indium oxide. *J. Catal.* **2018**, *361*, 313−321.

(30) Thommes, M.; Kaneko, K.; Neimark, A. V.; Olivier, J. P.; Rodriguez-Reinoso, F.; Rouquerol, J.; Sing, K. S. W. Physisorption of gases, with special reference to the evaluation of surface area and pore size distribution (IUPAC Technical Report). *Pure Appl. Chem.* **2015**, *87* (9−10), 1051−1069.

(31) https://srdata.nist.gov/xps/EngElmSrchQuery.aspx?EType=PE&CSOpt=Retri_ex_dat&Elm=In (accessed October 2023).

(32) https://www.thermofisher.com/se/en/home/materials-science/learning-center/periodic-table/other-metal/indium.html (accessed October 2023).

(33) Sharma, P.; Hoang Ho, P.; Shao, J.; Creaser, D.; Olsson, L. Role of ZrO2 and CeO2 support on the In2O3 catalyst activity for CO2 hydrogenation. *Fuel* **2023**, *331*, No. 125878.

(34) (a) Su, Y.-M.; Kuo, Y.-L.; Lin, C.-M.; Lee, S.-F. One-step fabrication of tetragonal ZrO2 particles by atmospheric pressure plasma jet. *Powder Technol.* **2014**, *267*, 74−79. (b) Basahel, S. N.; Ali, T. T.; Mokhtar, M.; Narasimharao, K. Influence of crystal structure of nanosized ZrO2 on photocatalytic degradation of methyl orange. *Nanoscale Res. Lett.* **2015**, *10* (1), 73.

(35) Lackner, P.; Zou, Z.; Mayr, S.; Diebold, U.; Schmid, M. Using photoelectron spectroscopy to observe oxygen spillover to zirconia. *Phys. Chem. Chem. Phys.* **2019**, *21* (32), 17613−17620.

(36) Sun, K.; Shen, C.; Zou, R.; Liu, C.-J. Highly active Pt/In2O3-ZrO2 catalyst for CO2 hydrogenation to methanol with enhanced CO

https://doi.org/10.1021/acs.energyfuels.3c04721
Energy Fuels XXXX, XXX, XXX−XXX

tolerance: The effects of ZrO2. *Applied Catalysis B: Environmental* **2023**, *320*, No. 122018.
(37) Busca, G.; Lorenzelli, V. Infrared spectroscopic identification of species arising from reactive adsorption of carbon oxides on metal oxide surfaces. *Materials Chemistry* **1982**, *7* (1), 89−126.
(38) Reyes, L. M. *Surface Adsorption Studies of CO2 and H2 on Defected Indium Oxide: Insights into Gas-Phase Heterogeneous Photocatalysis*; University of Toronto, 2017; https://tspace.library.utoronto.ca/handle/1807/97195 (accessed December 2023).
(39) Collins, S. E.; Baltanás, M. A.; Bonivardi, A. L. Infrared Spectroscopic Study of the Carbon Dioxide Adsorption on the Surface of Ga2O3 Polymorphs. *J. Phys. Chem. B* **2006**, *110* (11), 5498−5507.
(40) Tsoukalou, A.; Serykh, A. I.; Willinger, E.; Kierzkowska, A.; Abdala, P. M.; Fedorov, A.; Müller, C. R. Hydrogen dissociation sites on indium-based ZrO2-supported catalysts for hydrogenation of CO2 to methanol. *Catal. Today* **2022**, *387*, 38−46.
(41) Yan, T.; Li, N.; Wang, L.; Ran, W.; Duchesne, P. N.; Wan, L.; Nguyen, N. T.; Wang, L.; Xia, M.; Ozin, G. A. Bismuth atom tailoring of indium oxide surface frustrated Lewis pairs boosts heterogeneous CO2 photocatalytic hydrogenation. *Nat. Commun.* **2020**, *11* (1), 6095.
(42) Cárdenas-Arenas, A.; Quindimil, A.; Davó-Quiñonero, A.; Bailón-García, E.; Lozano-Castelló, D.; De-La-Torre, U.; Pereda-Ayo, B.; González-Marcos, J. A.; González-Velasco, J. R.; Bueno-López, A. Isotopic and in situ DRIFTS study of the CO2 methanation mechanism using Ni/CeO2 and Ni/Al2O3 catalysts. *Applied Catalysis B: Environmental* **2020**, *265*, No. 118538.
(43) Yang, B.; Li, L.; Jia, Z.; Liu, X.; Zhang, C.; Guo, L. Comparative study of CO2 hydrogenation to methanol on cubic bixbyite-type and rhombohedral corundum-type indium oxide. *Chin. Chem. Lett.* **2020**, *31* (10), 2627−2633.
(44) Numpilai, T.; Kidkhunthod, P.; Cheng, C. K.; Wattanakit, C.; Chareonpanich, M.; Limtrakul, J.; Witoon, T. CO2 hydrogenation to methanol at high reaction temperatures over In2O3/ZrO2 catalysts: Influence of calcination temperatures of ZrO2 support. *Catal. Today* **2021**, *375*, 298−306.
(45) (a) Dang, S.; Gao, P.; Liu, Z.; Chen, X.; Yang, C.; Wang, H.; Zhong, L.; Li, S.; Sun, Y. Role of zirconium in direct CO2 hydrogenation to lower olefins on oxide/zeolite bifunctional catalysts. *J. Catal.* **2018**, *364*, 382−393. (b) Dou, M.; Zhang, M.; Chen, Y.; Yu, Y. Theoretical study of methanol synthesis from CO2 and CO hydrogenation on the surface of ZrO2 supported In2O3 catalyst. *Surf. Sci.* **2018**, *672*−*673*, 7−12.
(46) Chen, P.; Tao, L.; Zhu, J.; Zhao, G.; Liu, Y.; Lu, Y. Morphology-Controllable Hexagonal-Phase Indium Oxide In Situ Structured onto a Thin-Felt Al2O3/Al-Fiber for the Hydrogenation of CO2 to Methanol. *Energy Technol.* **2019**, *7* (3), No. 1800747.
(47) Chou, C.-Y.; Lobo, R. F. Direct conversion of CO2 into methanol over promoted indium oxide-based catalysts. *Applied Catalysis A: General* **2019**, *583*, No. 117144.

https://doi.org/10.1021/acs.energyfuels.3c04721
Energy Fuels XXXX, XXX, XXX−XXX